

SDUM: A Scalable Deep Unrolled Model for Universal MRI Reconstruction

Puyang Wang^{1,*} Pengfei Guo^{2,*} Keyi Chai¹ Jinyuan Zhou¹ Daguang Xu² Shanshan Jiang¹

¹Johns Hopkins University ²NVIDIA

*Equal contribution

Clinical MRI encompasses diverse imaging protocols—spanning anatomical targets (cardiac, brain, knee), contrasts (T1, T2, mapping), sampling patterns (Cartesian, radial, spiral, kt-space), and acceleration factors—yet current deep learning reconstructions are typically protocol-specific, hindering generalization and deployment. We introduce Scalable Deep Unrolled Model (SDUM), a universal framework combining a Restormer-based reconstructor, learned coil sensitivity map estimator (CSME), sampling-aware weighted data consistency (SWDC), universal conditioning (UC) on cascade index and protocol metadata, and progressive cascade expansion training. SDUM exhibits foundation-model-like scaling behavior: reconstruction quality follows $\text{PSNR} \sim \log(\text{parameters})$ with correlation $r=0.986$ ($R^2=0.973$) up to 18 cascades, demonstrating predictable performance gains with model depth. A single SDUM trained on heterogeneous data achieves state-of-the-art results across all four CMRxRecon2025 challenge tracks—multi-center, multi-disease, 5T, and pediatric—without task-specific fine-tuning, surpassing specialized baselines by up to +1.0 dB. On CMRxRecon2024, SDUM outperforms the winning method PromptMR+ by +0.55 dB; on fastMRI brain, it exceeds PC-RNN by +1.8 dB. Ablations validate each component: SWDC +0.43 dB over standard DC, per-cascade CSME +0.51 dB, UC +0.38 dB. These results establish SDUM as a practical path toward universal, scalable MRI reconstruction.

Code and models will be released at: <https://github.com/NVIDIA-Medtech>

1. Introduction

Magnetic Resonance Imaging (MRI) reconstruction is an ill-posed inverse problem whose real-world manifestations span a vast range of anatomical targets (cardiac, brain, knee, abdomen), contrasts (T1, T2, FLAIR, diffusion, mapping sequences), sampling trajectories (Cartesian, radial, spiral, kt-space), and acceleration factors. While recent deep learning methods [16, 37, 9, 1, 40] have delivered strong performance in controlled settings, they typically fracture along protocol boundaries: a model trained for one sampling mask or acceleration often degrades when the acquisition changes. This brittleness hinders deployment in multi-site, multi-protocol clinical environments and motivates a *single, universally applicable* reconstruction model—analogous in spirit to foundation models in vision [8, 24, 34] and language—that can robustly handle heterogeneous inputs without per-protocol retraining.

The heterogeneity challenge. Clinical MRI workflows routinely acquire diverse contrasts with Cartesian, radial, spiral, or kt sampling and a broad range of acceleration factors. Scanner field strengths, coil arrays, and patient populations vary across sites. Yet most learning-based reconstructions are protocol-specific: they require bespoke tuning, separate training datasets, or architectural modifications when protocols shift. This imposes operational burden,

slows translation from research to clinic, and limits the practical utility of learned reconstructors.

The scaling-law gap. In adjacent domains, scaling laws [22, 18, 55]—empirical relationships quantifying how error decays with parameters, data, or compute—have become a practical compass for model design and resource allocation. MRI reconstruction lacks such guidance. Practitioners must rely on trial-and-error to decide whether to invest in wider backbones, deeper cascade unrolling, larger training sets, or additional compute, with no principled understanding of returns or saturation points.

Limitations of existing approaches. Current attempts at universal MRI reconstruction remain incomplete. Many deep unrolled models [16, 1] employ a scalar data-consistency (DC) weight that ignores sampling-pattern-specific density and noise characteristics. Conditioning mechanisms—when present—are often ad hoc or task-specific [47]. Coil sensitivity maps (CSMs) are typically precomputed and fixed, limiting robustness to motion and field inhomogeneities. Architectures may not be simultaneously resolution-agnostic and coil-flexible, restricting their applicability.

Our approach: SDUM. We introduce the Scalable Deep Unrolled Model (SDUM), a universal framework that addresses these limitations through

arXiv:2512.17137v1 [cs.CV] 19 Dec 2025

five key innovations:

1. **Restormer-based reconstruction backbone:** We adopt Restormer [53]’s Multi-Dconv Head Transposed Attention (MDTA) and Gated-Dconv Feedforward Network (GDFN), which jointly capture long-range dependencies and local structures with favorable memory and computational efficiency. A shallow two-stage pyramid (one down/up-sample) preserves high-resolution detail while enabling global context aggregation.
2. **Learned coil sensitivity map estimation (CSME):** A U-Net-based estimator refines CSMs at each cascade, mitigating errors from motion, noise, and field inhomogeneities without relying on autocalibration regions [33, 42].
3. **Sampling-aware weighted data consistency (SWDC):** Instead of a scalar DC weight, we learn spatially varying k-space weight maps conditioned on the sampling pattern, enabling mask-specific and density-aware fidelity enforcement.
4. **Universal conditioning (UC):** Sinusoidal embeddings of cascade index t and protocol metadata (mask type, acceleration, modality) are mapped through small MLPs and injected into every Restormer block, allowing a single model to adapt its behavior across diverse acquisitions [32, 31].
5. **Progressive cascade expansion:** Training proceeds by doubling interior cascades while fixing endpoints, stabilizing optimization and reusing learned weights as depth increases [3, 23].

We train SDUM on heterogeneous CMRxRecon and fastMRI data, covering cardiac (BlackBlood, Cine, Flow2d, LGE, Mapping, Perfusion, T1rho, T1w, T2w, Aorta, Tagging) and brain (AXT1, AXT2, AXFlair, AXT1POST) protocols with Cartesian and non-Cartesian sampling. On the CMRxRecon2025 challenge, evaluating generalization to unseen centers, diseases, 5T field strength, and pediatric populations, SDUM achieves state-of-the-art performance across all four tracks with a single model and no task-specific fine-tuning, exceeding specialized baselines by up to +1.0 dB. On CMRxRecon2024, SDUM surpasses the winning method PromptMR+ [47] by +0.55 dB. On fastMRI brain [54], it exceeds the winning solution PC-RNN [5] by +1.8 dB. Extensive ablations validate each design choice: SWDC yields +0.43 dB over standard DC, per-cascade CSME adds +0.51 dB, and UC contributes +0.38 dB. Beyond headline metrics, we conduct (to our knowledge) the **first scaling-laws study for MRI reconstruction**. Sweeping cascade depth T from 1 to 18, we observe that reconstruction quality follows $\text{PSNR} \sim \log(\text{parameters})$ with correlation $r=0.986$ ($R^2=0.973$), demonstrating predictable and consistent gains with no early saturation. This

provides a practical guide for trading compute against reconstruction fidelity.

2. Related Work

Classical and deep learning MRI reconstruction.

Classical accelerated MRI reconstruction employs compressed sensing [27], parallel imaging (SENSE [33], GRAPPA [13], ESPIRiT [42]), and dynamic imaging methods [12, 29]. Deep unrolled models (DUMs) [37, 16, 9, 1, 40] integrate iterative optimization into neural networks, alternating data-consistency (DC) and learned regularization steps. Related approaches include KIKI-Net [11], DeepComplexMRI [45], PC-RNN [5], and Plug-and-Play/RED frameworks [43, 35, 56]. Most unrolled models use scalar DC weights; our SWDC learns spatially varying k-space weights conditioned on sampling patterns. E2E-VarNet [40] jointly learns reconstruction and sensitivity estimation, inspiring our learned CSME approach.

Architectures. U-Net [36] and its variants (Attention U-Net [28], nnU-Net [19]) remain foundational in medical imaging. Vision Transformers [8, 26] and restoration transformers (SwinIR [25], IPT [6], Restormer [53]) capture long-range dependencies efficiently. We adopt Restormer for its favorable memory/compute trade-off and global-local modeling. Diffusion models [17, 39, 7, 20] offer generative priors but require many inference steps; we focus on efficient feed-forward unrolling.

Conditioning and universality. Conditional normalization techniques (FiLM [32], CIN [10], AdaLN [31], SPADE [30]) enable task adaptation. In MRI, PromptMR+ [47] and HierAdaptMR [50] use conditioning for multi-contrast and cross-center reconstruction. Foundation models [34, 24] demonstrate strong generalization in vision; we extend this paradigm to physics-informed MRI reconstruction.

Scaling and training. Scaling laws [22, 18, 55] quantify performance vs. parameters/data/compute in NLP and vision, guiding resource allocation. Prior work has shown that increasing unrolled depth (number of cascades) is important for reconstruction performance: ReconFormer [14] demonstrated this with recurrent transformers, and similar findings were reported for deep unrolled models [48]. For training, our cascade expansion applies progressive training [3, 23] which stabilizes optimization to deep unrolling.

3. Methods

3.1. Problem Formulation

MRI reconstruction aims to recover an image $x \in \mathbb{C}^{H \times W}$ from undersampled multi-coil k -space

measurements $y \in \mathbb{C}^{C \times H \times W}$ with C receiver coils. The forward model is

$$y = M \cdot \mathcal{F}(S \cdot x) + n, \quad (1)$$

where S denotes coil sensitivity maps, \mathcal{F} is the Fourier transform, M is a binary sampling mask, and n is acquisition noise. Real-world protocols vary in anatomy, modality (T1, T2, mapping), sampling pattern (Cartesian, radial, spiral, kt), and acceleration, so the model must handle heterogeneous acquisition conditions.

We pose reconstruction as the standard DC plus regularization problem

$$\hat{x} = \operatorname{argmin}_x \left(\frac{1}{2} \|M \cdot \mathcal{F}(S \cdot x) - y\|_2^2 + \lambda R(x) \right),$$

where \hat{x} is the reconstructed image. The first term enforces data consistency via the ℓ_2 norm. The regularizer $R(x)$ encodes priors such as total variation, wavelet sparsity, or a learned deep prior, with λ balancing DC and regularization. This objective is typically solved by first-order or splitting methods such as gradient or proximal gradient and ADMM, depending on $R(x)$.

Deep Unrolled Reconstruction. Let $A = M \cdot \mathcal{F}$ and $A^H = \mathcal{F}^{-1} \cdot M^H$. Unrolled methods realize T iterations that alternate a *data-consistency (DC)* step driven by the forward model and a *regularization/reconstruction* step parameterized by a neural network. We consider proximal-gradient (ISTA) and variable-splitting (ADMM) templates and observe no statistically significant difference when using deep priors, so we adopt proximal-gradient for simplicity.

Proximal-gradient unrolling. Starting from $x^{(0)}$ (for example, the zero-filled image), cascade $t \in \{0, \dots, T-1\}$ performs

$$z^{(t)} = x^{(t)} - \tau_t S^H A^H (A S \cdot x^{(t)} - y), \quad (2)$$

$$x^{(t+1)} = D_{\theta}^{(t)}(z^{(t)}), \quad (3)$$

where τ_t is a learnable step size (DC weight) and $D_{\theta^{(t)}}$ is a learnable proximal surrogate (for example, U-Net, Restormer). Step (2) enforces DC and (3) injects the learned prior.

End-to-end model. After T cascades,

$$\hat{x} = \Phi_{\Theta}(y, M, S) = x^{(T)}, \quad \Theta = \{\theta^{(t)}\}_{t=0}^{T-1}, \quad (4)$$

with optional feature sharing across t and optional conditioning inputs (for example, cascade index, modality, acceleration, mask identity) passed to $D_{\theta^{(t)}}$. The unrolled computation can be trained end-to-end to minimize a reconstruction loss (for example, ℓ_1 , ℓ_2 , SSIM) over heterogeneous acquisition conditions.

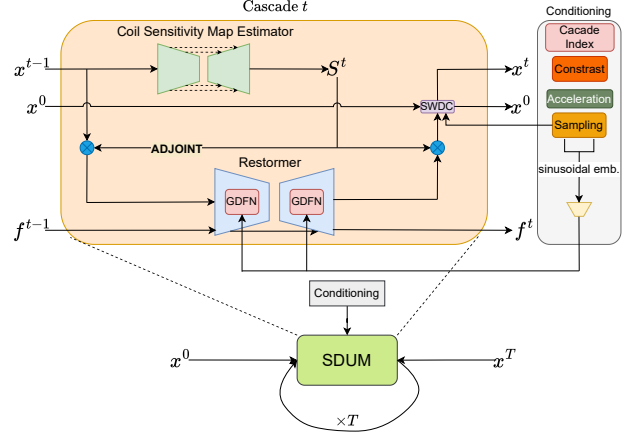


Figure 1 | **SDUM overview.** Each cascade combines a Restormer-based reconstructor, a learned CSME, sampling-aware weighted data consistency (SWDC), and universal conditioning (UC) on cascade index and protocol metadata.

3.2. Scalable Deep Unrolled Models

Fig. 1 provides an overview of the SDUM architecture. Deep unrolled MRI reconstruction methods rely on the fidelity of precomputed coil sensitivity maps (CSMs), whether obtained via SENSE calibration or estimated from an auto-calibration signal (ACS) region. In practice, CSMs are inevitably imperfect due to noise, motion, and field inhomogeneities, which can limit reconstruction quality. Moreover, increasing the number of cascades T further deepens the unrolled network, making optimization more challenging and increasing memory and compute cost.

We adopt a deep-unrolled architecture with T cascades. Each cascade comprises (i) a Restormer-based image reconstructor, (ii) a U-Net-based coil-sensitivity map estimator (CSME) that refines CSMs during reconstruction and does not rely on ACS regions, and (iii) a sampling-aware data-consistency operator that enforces the forward model with mask-dependent weighting in k-space. We introduce two key enhancements:

Adaptive unrolling with cascade skip connections. Each cascade receives not only the output of the previous stage, but also skip connections of decoder feature at downsampling level f_t from previous cascade. This mitigates vanishing gradients, facilitates training deeper models, and supports effective reuse of intermediate features.

Adjacent slice/frame input. For dynamic (eg. cinematic cardiac MRI) and 3D volumetric MRI, each cascade can access temporally or spatially adjacent frames. These inputs are fed into the reconstructor alongside the current slice, enabling the model to leverage temporal redundancy or 3D anatomical context.

3.3. Restormer for MRI reconstruction

Undersampling artifacts fold information over large spatial extents, while coil sensitivity and tissue boundaries induce fine local structure. A reconstructor must therefore (i) propagate *global* context to untangle aliasing and (ii) preserve *local* edges and textures to avoid hallucination. Purely convolutional U-Nets require depth or aggressive downsampling for long-range interactions, and windowed Transformers restrict cross-window communication. We adopt Restormer [52] because its Multi-Dconv Head Transposed Attention (MDTA) and Gated-Dconv Feedforward Network (GDFN) jointly capture non-local and local dependencies with favorable memory and compute cost. Specifically, MDTA operates over $C \times C$ rather than $(HW) \times (HW)$, yielding complexity $O(HW \cdot C^2)$ while retaining non-local context, and its convolutional bias matches the piecewise-smooth statistics of MR images with sharp boundaries. In this work, we make the following observations regarding Restormer as the reconstruction backbone.

Receptive field & downsampling. Empirically, two stages with a single down/upsample yield higher PSNR/SSIM. high-resolution processing limits abstraction loss, while MDTA still provides long-range interaction. Deeper pyramids widen the receptive field but increase over-smoothing and hallucination risk.

Unrolling efficiency. A shallow but wider per-cascade backbone stabilizes deep unrolling. it enables more cascades or larger input size without gradient accumulation, improving DC–prior interplay and gradient quality.

MRI-specific choices. We use two channels (real/imag), residual scaling around blocks, and layer-wise normalization to handle scanner/protocol intensity shifts; no positional encodings are used.

Implementation. We use two stages (one down, one up) with MDTA+GDFN blocks, long and short skips, and width tuned to fit maximum GPU memory, allowing large input K-space data for stable unrolled training.

Proximal-gradient unrolling with learned CSM and Restormer. At cascade $t \in \{0, \dots, T-1\}$, we estimate coil sensitivities with a U-Net CSME and then apply DC and a Restormer prior:

$$S^{(t)} = \text{Norm}\left(\text{CSME}_{\phi_t}(x^{(t)})\right), \quad (5)$$

$$z^{(t)} = x^{(t)} - \tau_t S^{(t)H} A^H \left(A(S^{(t)} \cdot x^{(t)}) - y \right), \quad (6)$$

$$x^{(t+1)} = \text{Restormer}_{\theta_t}(z^{(t)}), \quad (7)$$

where $A = M\mathcal{F}$, τ_t is a learnable DC step size, and $\text{Norm}(\cdot)$ enforces per-pixel coil normalization (e.g.,

$\sum_c |S_c|^2 = 1$). In (6) $S^{(t)}$ is treated as fixed within the t -th DC step, and $\text{Restormer}_{\theta_t}$ serves as the learned proximal operator.

3.4. Sampling-aware Weighted Data Consistency

In this study, we enhance the gradient-based data consistency (DC) update mechanism within each cascade by incorporating a *sampling-aware* weighting map in the k -space domain. This weighting map is designed to be contingent upon the diverse sampling masks, thereby facilitating an adaptive DC approach that accommodates variable sampling densities across distinct k -space regions. Recall that $A = M\mathcal{F}$ denotes masked Fourier encoding and $S^{(t)}$ is the coil-sensitivity map (CSM) estimated by the CSME in cascade t . The standard DC gradient in cascade t is

$$g_{\text{DC}}^{(t)} = S^{(t)H} A^H \left(A(S^{(t)} \cdot x^{(t)}) - y \right), \quad (8)$$

leading to the update $z^{(t)} = x^{(t)} - \tau_t g_{\text{DC}}^{(t)}$.

Weighted residual in k -space. Let $w^{(t)} \in \mathbb{R}^{H \times W}$ be a nonnegative weight map defined in k -space (broadcast across coils), with $w^{(t)} = 0$ on unsampled locations. We form a weighted residual

$$r_w^{(t)} = w^{(t)} \odot \left(A(S^{(t)} \cdot x^{(t)}) - y \right), \quad (9)$$

and replace (8) by

$$g_{\text{SWDC}}^{(t)} = S^{(t)H} A^H (r_w^{(t)}) \quad (10)$$

yielding the SWDC update $z^{(t)} = x^{(t)} - \tau_t g_{\text{SWDC}}^{(t)}$. When $w^{(t)} = M$, (10) recovers the standard DC. Empirical evidence suggests that the parameter τ_t may be assigned a value of 1 without compromising the efficacy of the sampling-aware capability. As shown in Fig. 2, the SWDC module learns distinct weight maps tailored to uniform, Gaussian, and radial sampling patterns.

Construction of $w^{(t)}$. The learnable parameter $w^{(t)}$ is initialized with maximum dimension $H \times W$, and a center crop is applied to match the dimensions of y . Our objective is to enable $w^{(t)}$ to accurately represent the sampling density and emphasize the central k -space region. To enhance sampling awareness further, we develop distinct $w_s^{(t)}$ for varying sampling patterns s (uniform, Gaussian, radial, etc.). This approach enables sampling-pattern-specific DC layers.

3.5. Universal Conditioning Mechanism

Clinical MRI protocols vary widely across mask types (variable density, kt-radial, Poisson, etc.), acquisition trajectories (e.g., Cartesian, non-Cartesian,

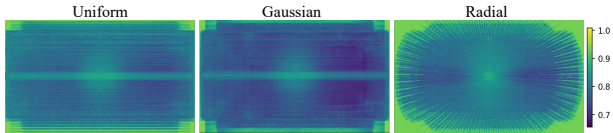


Figure 2 | **Example learned sampling-aware data-consistency** weight maps showing spatial adaptation to sampling patterns.

single/multi-shot, kt sampling), and acceleration factors. Separate models per protocol are impractical at scale and degrade robustness when the deployment distribution shifts. Moreover, deep unrolled reconstructions are *procedural*: early cascades behave like data-consistency regularizer while later cascades act more like powerful reconstructor. Providing each cascade with (i) its position in the unrolling and (ii) a compact descriptor of the acquisition allows a *single* model to adapt its behavior on the fly—tightening DC early, relaxing it later, and adjusting priors to the sampling regime—without proliferating model variants.

Universal Conditioning (UC) for time & protocol. We condition every cascade on (i) its cascade index t and (ii) a discrete protocol label y that encodes mask type, acquisition type, and acceleration factor. Both are mapped by a sinusoidal embedding followed by a small MLP and *summed* to form a single conditioning vector that is injected into all transformer blocks.

Let $\phi(\cdot): \mathbb{R} \rightarrow \mathbb{R}^{d_0}$ denote a sinusoidal encoder and let $h_t, h_y: \mathbb{R}^{d_0} \rightarrow \mathbb{R}^d$ be two-layer MLPs,

$$c = h_t(\phi(t)) + h_y(\phi(y)) \in \mathbb{R}^d. \quad (11)$$

Injection into Transformer blocks. Let $f_\ell^{(t)} \in \mathbb{R}^{H_\ell \times W_\ell \times C_\ell}$ be features at layer ℓ in cascade t . Each transformer block receives c and applies attention and a gated depthwise FFN (GDFN) with an *additive, spatially broadcast* bias derived from c :

$$\tilde{f}_\ell^{(t)} = \text{MDTA}(f_\ell^{(t)}) + f_\ell^{(t)}, \quad (12)$$

$$f_{\ell+1}^{(t)} = \text{GDFN}(\tilde{f}_\ell^{(t)}) + B_\ell(c), \quad (13)$$

where $B_\ell(c)$ produces a C_ℓ -dimensional vector that is broadcast across (H_ℓ, W_ℓ) using single linear layer. The same c is passed (via a timestep-aware sequential wrapper) to *all* encoder, decoder, and refinement blocks of each cascade in the Restormer.

3.6. Progressive Cascade Expansion

In unrolled reconstructions, the first cascade quickly restores k-space fidelity and the last consolidates the image prior, while most residual correction happens mid-trajectory. By fixing the endpoints and only

doubling interior cascades, we refine the discretization exactly where truncation error is largest—analogue to inserting midpoints in an ODE solver—without disturbing the learned boundary roles.

We train deep unrolled models with a curriculum that grows the cascade depth while reusing parameters to stabilize optimization. From a stage with T_{k-1} cascades, the next stage expands to $T_k = 2(T_{k-1} - 1)$, by keeping the first and last cascades fixed and *duplicating only the intermediate cascades*. This preserves the early/late “anchors” of the unrolled trajectory (data-consistency at the start and the final proximal stage), while refining the interior with finer granularity.

Let $\theta^{(t)}$ denote proximal (Restormer/UNet) weights, $\phi^{(t)}$ the CSME weights, τ_t the DC step sizes, and $w^{(t)}$ the SWDC weights at cascade index t . Define the index mapping $\pi_k: \{0, \dots, T_k - 1\} \rightarrow \{0, \dots, T_{k-1} - 1\}$ as

$$\pi_k(t) = \begin{cases} 0, & t=0, \\ T_{k-1}-1, & t=T_k-1, \\ 1 + \lfloor (t-1)/2 \rfloor, & \text{otherwise.} \end{cases}$$

Initialization at stage k is then

$$\begin{aligned} \theta^{(t)} &\leftarrow \theta_{\text{prev}}^{(\pi_k(t))}, & \phi^{(t)} &\leftarrow \phi_{\text{prev}}^{(\pi_k(t))}, \\ \tau_t &\leftarrow \tau_{\text{prev}}^{(\pi_k(t))}, & w^{(t)} &\leftarrow w_{\text{prev}}^{(\pi_k(t))}. \end{aligned} \quad (14)$$

Thus, $t = 0$ and $t = T_k - 1$ copy the previous endpoints unchanged, while each interior cascade $j \in \{1, \dots, T_{k-1} - 2\}$ is duplicated into two consecutive positions. This “end-fixed, middle-doubling” schedule warm-starts new depths from well-trained operating points, improves gradient flow across the unrolled chain, and empirically yields faster convergence at large T with no extra parameters introduced beyond the copied blocks. With $T_k = 2(T_{k-1} - 1)$, one can write $T_k = 2^k(T_0 - 2) + 2$ for a given base depth $T_0 \geq 2$.

4. Experiments

We evaluate our *foundation-style* MRI reconstruction model on multi-coil Cartesian and non-Cartesian protocols using the **CMRxRecon2024** challenge [44], **CMRxRecon2025** challenge [49], and **fastMRI multi-coil brain** benchmarks [54]. CMRxRecon2025 extends the 2024 challenge with domain shifts across vendors and anatomies, while fastMRI assesses cross-modality generalization. All datasets provide complex-valued multi-coil k-space measurements and corresponding ground-truth references. Unless stated otherwise, results are reported on the official validation splits or challenge leaderboard evaluations. Reconstruction quality is measured by SSIM \uparrow , PSNR \uparrow , and NMSE \downarrow . Additional details on experiment setup and model training can be found in the supplementary material.

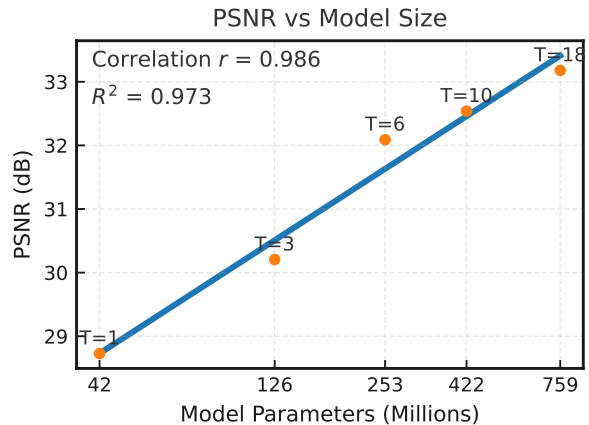
Table 1 | **Ablation study on CMRxRecon2025 challenge.** Results are reported on the official leaderboard of regular Task 1 (multi-center evaluation). Default configurations are marked in gray.

(a) Backbone variants. All backbones are configured to $T=6$.				(b) Effect of down-sampling (DS) layers on reconstruction accuracy.				(c) Single-cascade capacity scaling. We study different network widths within a single cascade.			
Backbone	SSIM	PSNR	NMSE	# DS layers	SSIM	PSNR	NMSE	Param.	SSIM	PSNR	NMSE
U-Net [36]	0.811	28.734	0.032	4	0.872	31.544	0.019	7.2 M	0.784	27.605	0.042
DiT [31]	0.825	29.542	0.028	3	0.877	31.787	0.018	13.4 M	0.803	28.271	0.036
TAU [41]	0.873	31.597	0.018	2	0.881	32.090	0.017	42.2 M	0.814	28.728	0.033
Restormer [53]	0.881	32.090	0.017	1	Training Failed			78.7 M	0.821	28.978	0.031

(d) CSME variants. <i>Multiple</i> setting equips each cascade with its own CSME.				(e) Effect of UC and iterative reconstruction. Iter. denotes the number of iterations.				(f) Data Consistency (DC) layer variants. WDC denotes the Weighted Data Consistency.					
CSME	SSIM	PSNR	NMSE	T	Iter.	UC	SSIM	PSNR	NMSE	DC layer	SSIM	PSNR	NMSE
Single	0.840	29.694	0.026	1	3	✗	0.835	29.693	0.027	Simple Learnable	0.872	31.661	0.018
Multiple	0.845	30.205	0.025	1	3	✓	0.843	30.071	0.025	WDC	0.877	31.787	0.017
				3	1	✓	0.845	30.205	0.025	SWDC	0.881	32.090	0.017

4.1. Baselines

We benchmark SDUM against a broad spectrum of reconstruction methods. On the fastMRI multi-coil brain benchmark, we compare against widely adopted baselines from prior work, including classical Compressed Sensing (CS) [27], U-Net [36], D5C5 [37], KIKI-Net [11], VN [16], VS-Net [9], ComplexMRI [45], and PC-RNN [5] (**fastMRI challenge winning solution**). These methods trace the evolution from sparsity-driven optimization to learned unrolled and recurrent designs. For the CMRxRecon2024 and CMRxRecon2025 challenges [49], we follow the official evaluation protocols and compare against the top-ranking leaderboard methods¹² across all subtasks. Representative contenders include PromptMR+ [47] (**CMRxRecon2024 winning solution**), Hamedani *et al.* [2], vSHARP with ARN [51], IMR [44], Shen *et al.* [38], HierAdaptMR [50], and GENRE-CMR [15]. These models encompass a diverse range of architectural paradigms, spanning physics-guided unrolled networks, hierarchical transformer priors, and recurrent refinement schemes and covering the current state of the art in MRI reconstruction. Together, these baselines provide a comprehensive comparison for evaluating the generalization and scalability of SDUM across anatomy, MR sequences, sampling patterns, and acceleration regimes.

Figure 3 | **Scaling behavior of unrolled depth T for reconstruction performance.**

4.2. Ablation Study

We conduct ablations on the CMRxRecon2025 challenge validation leaderboard to investigate the model components in the proposed SDUM. Results are summarized in Table 1, and scaling behaviors with respect to cascade depth are analyzed in Fig. 3.

Backbone variants. We evaluate different reconstruction backbones, including U-Net [36], DiT [31], TAU [41], and Restormer [53], using $T=6$ cascades with approximately the same number of trainable parameters. Restormer achieves the best overall performance (Table 1a) by coupling efficient global attention with strong local modeling. Its Multi-Dconv Head Transposed Attention (MDTA) aggregates long-range dependencies with linear spatial complexity, while

¹<https://www.synapse.org/Synapse:syn54951257/wiki/627936>

²<https://www.synapse.org/Synapse:syn59814210/wiki/631022>

Table 2 | **Quantitative comparison on the CMRxRecon2025 challenge.** Results are reported on the official leaderboard across four subtasks. SDUM is configured to $T=18$. Leaderboard results are current as of Nov. 13, 2025.

Regular Task 1: Multi-center evaluation				Regular Task 2: Multiple diseases evaluation				Special Task 1: 5T evaluation				Special Task 2: Pediatric imaging evaluation			
Method	SSIM	PSNR	NMSE	Method	SSIM	PSNR	NMSE	Method	SSIM	PSNR	NMSE	Method	SSIM	PSNR	NMSE
HierAdaptMR [50]	0.870	31.702	0.019	HierAdaptMR [50]	0.864	32.520	0.021	HierAdaptMR [50]	0.888	33.290	0.018	GENRE-CMR [15]	0.872	31.656	0.033
Shen <i>et al.</i> [38]	0.878	32.19	0.017	Shen <i>et al.</i> [38]	0.872	32.998	0.017	Shen <i>et al.</i> [38]	0.893	33.605	0.017	HierAdaptMR [50]	0.880	32.014	0.030
PromptMR+ [47]	0.891	32.919	0.014	PromptMR+ [47]	0.879	33.422	0.014	PromptMR+ [47]	0.895	33.824	0.016	Shen <i>et al.</i> [38]	0.887	32.436	0.028
SDUM (Ours)	0.895	33.179	0.014	SDUM (Ours)	0.880	33.538	0.014	SDUM (Ours)	0.901	34.225	0.015	SDUM (Ours)	0.905	33.478	0.020

Table 3 | **Quantitative comparison on the CM-RxRecon2024 challenge.** Results are reported on the official validation leaderboard across Task 1 and Task 2. SDUM is configured to $T=18$.

Task 1: Uniform ($4\times, 8\times, 10\times$)			
Method	SSIM	PSNR	NMSE
vSHARP w/ ARN [51]	0.910	34.449	0.022
Hamedani <i>et al.</i> [2]	0.912	34.522	0.022
PromptMR [46]	0.907	34.053	0.023
PromptMR+ (<i>12 cas.</i>) [48]	0.915	34.677	0.020
PromptMR+ (<i>32 cas.</i>) [47]	0.921	35.152	0.018
SDUM (Ours)	0.931	35.700	0.016
Task 2: k-t Gaussian/Radial/Uniform ($4\times-24\times$)			
Method	SSIM	PSNR	NMSE
IMR [57]	0.885	32.479	0.034
vSHARP w/ ARN [51]	0.888	32.712	0.033
PromptMR [46]	0.886	32.492	0.033
PromptMR+ (<i>12 cas.</i>) [48]	0.896	33.078	0.030
PromptMR+ (<i>32 cas.</i>) [47]	0.907	33.812	0.026
SDUM (Ours)	0.911	33.948	0.025

the Gated-Dconv Feed-Forward Network (GDFN) preserves local detail via convolutional bias—an ideal combination for MRI reconstruction, which demands both global context to unfold aliasing and precise spatial fidelity to retain coil-sensitive boundaries.

Down-sampling depth. We vary the number of down-sampling layers within each SDUM cascade with $T=6$. The number of down-sampling layers largely determines the model’s performance ceiling, as it directly controls the receptive field size. As shown in Table 1b, two layers provide the best balance between contextual coverage and spatial fidelity, achieving the highest PSNR (32.09 dB). Fewer layers hinder abstraction (training fails at one layer), while deeper hierarchies (three to four layers) lose fine texture fidelity. This supports our design choice of relatively shallow pyramids to preserve high-frequency anatomical detail.

Single-cascade capacity. To analyze intra-cascade scaling, we adjust network width (*i.e.*, the number of channels) in encoder and decoder from 7.2M to 78.7M parameters while fixing $T=1$. Table 1c shows model performance improves steadily up to ~ 42 M parameters (PSNR 28.73 dB) but saturates thereafter. This suggests that depth T (number of cascades) yields more efficient capacity scaling than width, motivating progressive cascade expansion as the preferred scaling axis.

CSME variants. We compare using a single coil sensitivity map estimator (CSME) once at the network input versus distinct estimators per cascade. Table 1d shows that the multi-CSME configuration improves PSNR by +0.51 dB. Progressive sensitivity refinement helps correct motion and field-inhomogeneity errors, reinforcing the advantage of jointly learning CSMs and image priors in the unrolled framework.

Data consistency formulations. We ablate different data consistency (DC) layers, including simple learnable DC, weighted DC (WDC), and our sampling-aware weighted DC (SWDC). Table 1f shows that SWDC achieves the best overall result, outperforming learnable DC (+0.43 dB). This demonstrates that incorporating sampling-pattern awareness improves fidelity across diverse settings during k-space gradient correction.

UC and iterative behavior. Table 1e studies the effect of the universal conditioning (UC) mechanism and iterative reconstruction under equal computing budgets. Comparing the first two rows, enabling UC consistently improves reconstruction quality (PSNR +0.38 dB), confirming that UC enhances adaptability across varying protocols. Comparing the second and third rows, three cascades without iterative refinement outperform a single cascade with three iterations at similar computing cost, indicating that under limited compute, increasing unrolled depth is more beneficial than additional iterations, while iterative refinement remains complementary for further gains.

Scaling behavior. Fig. 3 shows the scaling trend with respect to unrolled depth T . As the number of cascades increases, PSNR improves monotonically, following an approximately linear relationship with $\log(\# \text{ parameters})$ ($r=0.986$, $R^2=0.973$). This trend demonstrates that SDUM exhibits foundation-model-like scaling behavior, with predictable performance gains as unrolled depth T increases, and no sign of early saturation up to $T=18$.

Together, these analyses show that each design component contributes complementary improvements, yielding a scalable and stable unrolled reconstruction framework.

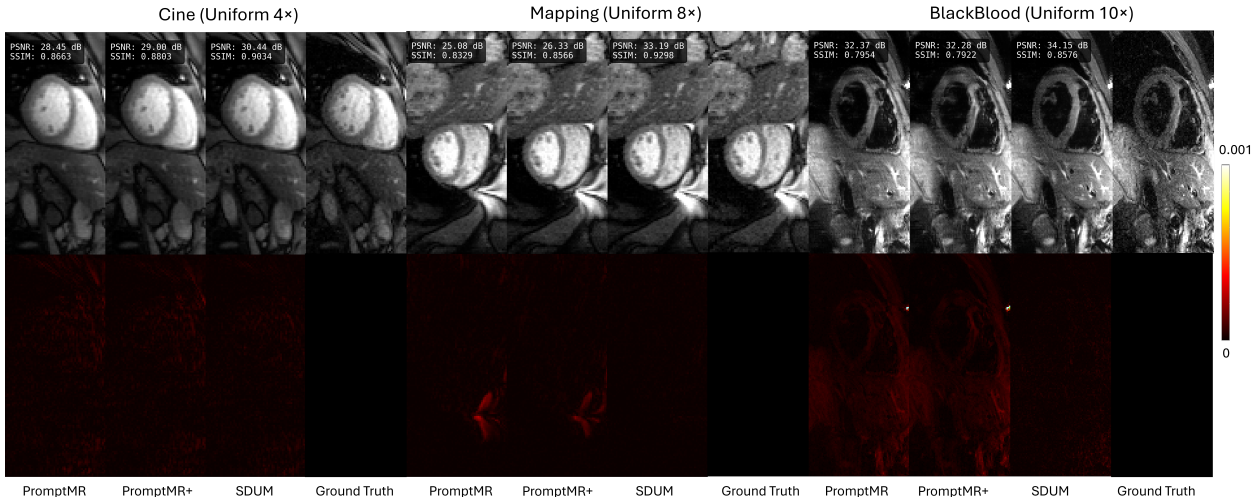


Figure 4 | **Qualitative comparison of MRI reconstruction methods across multiple cardiac imaging modalities.** Three representative cases from the CMRxRecon2024 Task 1 validation set demonstrate the superior performance of SDUM compared with PromptMR and PromptMR+.

4.3. Comparisons with State-of-the-Arts

CMRxRecon Challenge. Table 3 reports results on the official CMRxRecon2024 leaderboard across two subtasks. SDUM outperforms the 2024 winning method PromptMR+ [47] by 0.55 dB in Task 1. The proposed SDUM delivers consistently higher fidelity under both spatially uniform and temporally varying sampling conditions. These improvements stem from the synergy between the components discussed in Sec. 4.2, which jointly strengthen data fidelity and cross-protocol adaptability. Qualitative reconstructions (Fig. 4) further demonstrate clearer myocardial boundaries and reduced aliasing artifacts in dynamic cardiac regions.

Table 2 reports results on the CMRxRecon2025 leaderboard, which evaluates model generalization across unseen centers, diseases, field strengths, and age groups. Remarkably, a *single SDUM model* is used for all four subtasks without any task-specific fine-tuning, and it still achieves the highest SSIM and PSNR throughout, surpassing strong baselines including PromptMR+ (32 cas.) [47], HierAdaptMR [50], Shen *et al.* [38], and GENRE-CMR [15]. On Regular Task 1 (**multi-center generalization**), where both validation and test data come from entirely unseen medical centers, SDUM attains an absolute gain of +0.26 dB over the second place. On Regular Task 2 (**multi-disease evaluation**), which assesses robustness to unseen cardiovascular conditions with undisclosed disease labels, SDUM maintains superior performance. For the two special tracks (**5T** and **Pediatric**), SDUM generalizes even more strongly to field strengths and age distributions absent from training and exceeds the next-best methods by up to +1.0 dB PSNR, demonstrating strong adaptability to domain and physiolog-

Table 4 | **Quantitative comparison on the fastMRI multi-coil brain benchmark.** We follow the setting of PC-RNN [5] to report at acceleration factors of 4x and 6x using SSIM and PSNR metrics. SDUM is configured to T = 6.

Task: fastMRI Multi-coil Brain				
Method	4x		6x	
	SSIM	PSNR	SSIM	PSNR
CS [27]	0.904	35.2	0.851	31.2
U-Net [36]	0.944	36.3	0.925	34.3
VN [16]	0.938	36.2	0.900	32.6
VS-Net [9]	0.950	37.6	0.921	34.3
KIKI-Net [11]	0.956	37.9	0.935	35.3
D5C5 [37]	0.955	38.0	0.931	34.9
ComplexMRI [45]	0.953	37.9	0.933	35.2
PC-RNN [5]	0.971	40.8	0.962	38.9
SDUM (Ours)	0.979	42.6	0.973	40.8

ical shifts. These results highlight that SDUM trained as a single foundation-style reconstruction model sets a new SOTA on all four CMRxRecon2025 tracks.

fastMRI. Table 4 reports results on the fastMRI multi-coil brain benchmark at 4x and 6x acceleration. SDUM consistently outperforms prior learning-based methods. It exceeds the strong recurrent baseline PC-RNN [5] by +1.8 dB PSNR, validating the scalable unrolled Restormer backbone and sampling-aware weighted data consistency (SWDC). These results underscore that our model design, originally developed for cardiac MRI, generalizes robustly to other domains such as brain imaging, demonstrating the scalability and applicability of the foundation-style reconstruction paradigm. Additional experiment details and visualizations are provided in the supplementary material.

5. Discussion and Limitations

We present the first scaling-law analysis for MRI reconstruction, showing $\text{PSNR} \sim \log(\text{parameters})$ with $r=0.986$ ($R^2=0.973$) up to $T=18$ cascades without saturation. This predictable scaling—mirroring trends in language and vision foundation models [22, 18, 55]—suggests that increasing unrolled depth yields more efficient gains than widening cascades. SDUM thus establishes a foundation-model paradigm for MRI, achieving universal generalization across anatomy, contrast, sampling, and acceleration. Limitations include the fixed SWDC weight-map resolution, high training cost, and further scaling analysis beyond model size. Future work will extend SDUM to 3D volumetric reconstruction with anatomical priors [24], explore transformer architectures [26, 25] to enable further model scaling via model parallelism, integrate self-supervised learning to reduce reliance on fully sampled data, and pursue prospective clinical validation.

6. Conclusion

SDUM unifies Restormer-based reconstructor, learned CSME, SWDC, UC, and progressive cascade expansion into a single universal framework. It achieves state-of-the-art performance on all CMRxRecon 2024/2025 tracks and generalizes to fastMRI brain, demonstrating scalable, foundation-style MRI reconstruction across anatomies and protocols. Comprehensive ablations further verify that each component contributes complementary gains, highlighting the effectiveness and robustness of the overall design.

References

- [1] Hemant K Aggarwal, Merry P Mani, and Mathews Jacob. Modl: Model-based deep learning architecture for inverse problems. *IEEE Transactions on Medical Imaging*, 38(2):394–405, 2019.
- [2] Kian Anvari Hamedani, Narges Razizadeh, Shahabeddin Nabavi, and Mohsen Ebrahimi Moghaddam. An all-in-one approach for accelerated cardiac mri reconstruction. In *International Workshop on Statistical Atlases and Computational Models of the Heart*, pages 464–475. Springer, 2024.
- [3] Yoshua Bengio, Jérôme Louradour, Ronan Collobert, and Jason Weston. Curriculum learning. In *Proceedings of the 26th Annual International Conference on Machine Learning*, pages 41–48, 2009.
- [4] M Jorge Cardoso, Wenqi Li, Richard Brown, Nic Ma, Eric Kerfoot, Yiheng Wang, Benjamin Murrey, Andriy Myronenko, Can Zhao, Dong Yang, et al. Monai: An open-source framework for deep learning in healthcare. *arXiv preprint arXiv:2211.02701*, 2022.
- [5] Eric Z Chen, Puyang Wang, Xiao Chen, Terrence Chen, and Shanhui Sun. Pyramid convolutional rnn for mri image reconstruction. *IEEE Transactions on Medical Imaging*, 41(8):2033–2047, 2022.
- [6] Hanting Chen, Yunhe Wang, Tianyu Guo, Chang Xu, Yiping Deng, Zhenhua Liu, Siwei Ma, Chunjing Xu, Chao Xu, and Wen Gao. Pre-trained image processing transformer. In *Proceedings of the IEEE/CVF Conference on Computer Vision and Pattern Recognition*, pages 12299–12310, 2021.
- [7] Hyungjin Chung and Jong Chul Ye. Score-based diffusion models for accelerated mri. *Medical Image Analysis*, 80:102479, 2022.
- [8] Alexey Dosovitskiy, Lucas Beyer, Alexander Kolesnikov, Dirk Weissenborn, Xiaohua Zhai, Thomas Unterthiner, Mostafa Dehghani, Matthias Minderer, Georg Heigold, Sylvain Gelly, et al. An image is worth 16x16 words: Transformers for image recognition at scale. In *International Conference on Learning Representations*, 2021.
- [9] Jinming Duan, Jo Schlemper, Chen Qin, Cheng Ouyang, Wenjia Bai, Carlo Biffi, Ghalib Bello, Ben Statton, Declan P O’regan, and Daniel Rueckert. Vs-net: Variable splitting network for accelerated parallel mri reconstruction. In *International conference on medical image computing and computer-assisted intervention*, pages 713–722. Springer, 2019.
- [10] Vincent Dumoulin, Jonathon Shlens, and Manjunath Kudlur. A learned representation for artistic style. In *International Conference on Learning Representations*, 2017.
- [11] Taejoon Eo, Yohan Jun, Taeseong Kim, Jinseong Jang, Ho-Joon Lee, and Dosik Hwang. Kiki-net: cross-domain convolutional neural networks for reconstructing undersampled magnetic resonance images. *Magnetic resonance in medicine*, 80(5):2188–2201, 2018.
- [12] Li Feng, Robert Grimm, Kai Tobias Block, Hersh Chandarana, Sunghoon Kim, Jian Xu, Leon Axel, Daniel K Sodickson, and Ricardo Otazo. Golden-angle radial sparse parallel mri: combination of compressed sensing, parallel imaging, and golden-angle radial sampling for fast and flexible dynamic volumetric mri. *Magnetic Resonance in Medicine*, 72(3):707–717, 2014.
- [13] Mark A Griswold, Peter M Jakob, Robin M Heidemann, Mathias Nittka, Vladimir Jellus, Jianmin Wang, Berthold Kiefer, and Axel Haase. Generalized autocalibrating partially parallel acquisitions (grappa). *Magnetic Resonance in Medicine*, 47(6):1202–1210, 2002.
- [14] Pengfei Guo, Yiqun Mei, Jinyuan Zhou, Shanshan Jiang, and Vishal M Patel. Reconformer: Accelerated mri reconstruction using recurrent transformer. *IEEE transactions on medical imaging*, 43(1):582–593, 2023.

- [15] Kian Anvari Hamedani, Narges Razizadeh, Shahabeddin Nabavi, and Mohsen Ebrahimi Moghaddam. Genre-cmr: Generalizable deep learning for diverse multi-domain cardiac mri reconstruction. *arXiv preprint arXiv:2508.20600*, 2025.
- [16] Kerstin Hammernik, Teresa Klatzer, Erich Kobler, Michael P Recht, Daniel K Sodickson, Thomas Pock, and Florian Knoll. Learning a variational network for reconstruction of accelerated mri data. *Magnetic resonance in medicine*, 79(6):3055–3071, 2018.
- [17] Jonathan Ho, Ajay Jain, and Pieter Abbeel. Denoising diffusion probabilistic models. In *Advances in Neural Information Processing Systems*, pages 6840–6851, 2020.
- [18] Jordan Hoffmann, Sebastian Borgeaud, Arthur Mensch, Elena Buchatskaya, Trevor Cai, Eliza Rutherford, Diego de Las Casas, Lisa Anne Hendricks, Johannes Welbl, Aidan Clark, et al. Training compute-optimal large language models. *arXiv preprint arXiv:2203.15556*, 2022.
- [19] Fabian Isensee, Paul F Jaeger, Simon AA Kohl, Jens Petersen, and Klaus H Maier-Hein. nnu-net: a self-configuring method for deep learning-based biomedical image segmentation. *Nature Methods*, 18(2):203–211, 2021.
- [20] Ajil Jalal, Marius Arvinte, Giannis Daras, Eric Price, Alexandros G Dimakis, and Jonathan I Tamir. Robust compressed sensing mri with deep generative priors. In *Advances in Neural Information Processing Systems*, pages 14938–14954, 2021.
- [21] Keller Jordan, Yuchen Jin, Vlado Boza, You Jiacheng, Franz Cesista, Laker Newhouse, and Jeremy Bernstein. Muon: An optimizer for hidden layers in neural networks, 2024.
- [22] Jared Kaplan, Sam McCandlish, Tom Henighan, Tom B Brown, Benjamin Chess, Rewon Child, Scott Gray, Alec Radford, Jeffrey Wu, and Dario Amodei. Scaling laws for neural language models. *arXiv preprint arXiv:2001.08361*, 2020.
- [23] Tero Karras, Timo Aila, Samuli Laine, and Jaakko Lehtinen. Progressive growing of gans for improved quality, stability, and variation. In *International Conference on Learning Representations*, 2018.
- [24] Alexander Kirillov, Eric Mintun, Nikhila Ravi, Hanzi Mao, Chloe Rolland, Laura Gustafson, Tete Xiao, Spencer Whitehead, Alexander C Berg, Wan-Yen Lo, et al. Segment anything. In *Proceedings of the IEEE/CVF International Conference on Computer Vision*, pages 4015–4026, 2023.
- [25] Jingyun Liang, Jiezhong Cao, Guolei Sun, Kai Zhang, Luc Van Gool, and Radu Timofte. Swinir: Image restoration using swin transformer. In *Proceedings of the IEEE/CVF International Conference on Computer Vision Workshops*, pages 1833–1844, 2021.
- [26] Ze Liu, Yutong Lin, Yue Cao, Han Hu, Yixuan Wei, Zheng Zhang, Stephen Lin, and Baining Guo. Swin transformer: Hierarchical vision transformer using shifted windows. In *Proceedings of the IEEE/CVF International Conference on Computer Vision*, pages 10012–10022, 2021.
- [27] Michael Lustig, David L Donoho, Juan M Santos, and John M Pauly. Compressed sensing mri. *IEEE signal processing magazine*, 25(2):72–82, 2008.
- [28] Ozan Oktay, Jo Schlemper, Loic Le Folgoc, Matthew Lee, Mattias Heinrich, Kazunari Misawa, Kensaku Mori, Steven McDonagh, Nils Y Hammerla, Bernhard Kainz, et al. Attention u-net: Learning where to look for the pancreas. *arXiv preprint arXiv:1804.03999*, 2018.
- [29] Ricardo Otazo, Emmanuel Candès, and Daniel K Sodickson. Low-rank plus sparse matrix decomposition for accelerated dynamic mri with separation of background and dynamic components. *Magnetic Resonance in Medicine*, 73(3):1125–1136, 2015.
- [30] Taesung Park, Ming-Yu Liu, Ting-Chun Wang, and Jun-Yan Zhu. Semantic image synthesis with spatially-adaptive normalization. In *Proceedings of the IEEE/CVF Conference on Computer Vision and Pattern Recognition*, pages 2337–2346, 2019.
- [31] William Peebles and Saining Xie. Scalable diffusion models with transformers. In *Proceedings of the IEEE/CVF international conference on computer vision*, pages 4195–4205, 2023.
- [32] Ethan Perez, Florian Strub, Harm De Vries, Vincent Dumoulin, and Aaron Courville. Film: Visual reasoning with a general conditioning layer. In *Proceedings of the AAAI Conference on Artificial Intelligence*, 2018.
- [33] Klaas P Pruessmann, Markus Weiger, Markus B Scheidegger, and Peter Boesiger. Sense: sensitivity encoding for fast mri. *Magnetic Resonance in Medicine*, 42(5):952–962, 1999.
- [34] Alec Radford, Jong Wook Kim, Chris Hallacy, Aditya Ramesh, Gabriel Goh, Sandhini Agarwal, Girish Sastry, Amanda Askell, Pamela Mishkin, Jack Clark, et al. Learning transferable visual models from natural language supervision. In *International Conference on Machine Learning*, pages 8748–8763. PMLR, 2021.
- [35] Yaniv Romano, Michael Elad, and Peyman Milanfar. The little engine that could: Regularization by denoising (red). *SIAM Journal on Imaging Sciences*, 10(4):1804–1844, 2017.
- [36] Olaf Ronneberger, Philipp Fischer, and Thomas Brox. U-net: Convolutional networks for biomedical image segmentation. In *International Conference on Medical image computing and computer-assisted intervention*, pages 234–241. Springer, 2015.

- [37] Jo Schlemper, Jose Caballero, Joseph V Hajnal, Anthony Price, and Daniel Rueckert. A deep cascade of convolutional neural networks for mr image reconstruction. In *International conference on information processing in medical imaging*, pages 647–658. Springer, 2017.
- [38] Chushu Shen. “chushu shen (chushu) — synapse profile”. <https://www.synapse.org/Profile:3534520>, 2025. Accessed: 2025-11-12.
- [39] Yang Song, Jascha Sohl-Dickstein, Diederik P Kingma, Abhishek Kumar, Stefano Ermon, and Ben Poole. Score-based generative modeling through stochastic differential equations. In *International Conference on Learning Representations*, 2021.
- [40] Anuroop Sriram, Jure Zbontar, Tullie Murrell, Aaron Defazio, C Lawrence Zitnick, Nafissa Yakubova, Florian Knoll, and Patricia Johnson. End-to-end variational networks for accelerated mri reconstruction. *arXiv preprint arXiv:2004.06688*, 2020.
- [41] Cheng Tan, Zhangyang Gao, Lirong Wu, Yongjie Xu, Jun Xia, Siyuan Li, and Stan Z Li. Temporal attention unit: Towards efficient spatiotemporal predictive learning. In *Proceedings of the IEEE/CVF conference on computer vision and pattern recognition*, pages 18770–18782, 2023.
- [42] Martin Uecker, Peng Lai, Mark J Murphy, Patrick Virtue, Michael Elad, John M Pauly, Shreyas S Vasanaawala, and Michael Lustig. Espirit—an eigenvalue approach to autocalibrating parallel mri: where sense meets grappa. *Magnetic Resonance in Medicine*, 71(3):990–1001, 2014.
- [43] Singanallur V Venkatakrishnan, Charles A Bouman, and Brendt Wohlberg. Plug-and-play priors for model based reconstruction. In *2013 IEEE Global Conference on Signal and Information Processing*, pages 945–948. IEEE, 2013.
- [44] Fanwen Wang, Zi Wang, Yan Li, Jun Lyu, Chen Qin, Shuo Wang, Kunyuan Guo, Mengting Sun, Mingkai Huang, Haoyu Zhang, et al. Towards universal learning-based model for cardiac image reconstruction: Summary of the cmrxrecon2024 challenge. *arXiv preprint arXiv:2503.03971*, 2025.
- [45] Shanshan Wang, Huitao Cheng, Leslie Ying, Taohui Xiao, Ziwen Ke, Hairong Zheng, and Dong Liang. Deepcomplexmri: Exploiting deep residual network for fast parallel mr imaging with complex convolution. *Magnetic resonance imaging*, 68:136–147, 2020.
- [46] Bingyu Xin, Meng Ye, Leon Axel, and Dimitris N. Metaxas. Fill the k-space and refine the image: Prompting for dynamic and multi-contrast mri reconstruction. In *Statistical Atlases and Computational Models of the Heart. Regular and CMRxRecon Challenge Papers*, pages 261–273, Cham, 2024. Springer Nature Switzerland.
- [47] Bingyu Xin, Meng Ye, Leon Axel, and Dimitris N Metaxas. Enhanced deep unrolled models applied to the cmrxrecon2024 challenge. In *International Workshop on Statistical Atlases and Computational Models of the Heart*, pages 289–300. Springer, 2024.
- [48] Bingyu Xin, Meng Ye, Leon Axel, and Dimitris N Metaxas. Rethinking deep unrolled model for accelerated mri reconstruction. In *European Conference on Computer Vision*, pages 164–181. Springer, 2024.
- [49] Daryl Xu. Cmrrecon2025. Web page, <https://www.synapse.org/Synapse:syn59814210/wiki/628454>, 2025. Accessed: 2025-11-05.
- [50] Ruru Xu and Ilkay Oksuz. Hieradaptmr: Cross-center cardiac mri reconstruction with hierarchical feature adapters. *arXiv preprint arXiv:2508.13026*, 2025.
- [51] George Yiasemis, Nikita Moriakov, Jan-Jakob Sonke, and Jonas Teuwen. Deep multi-contrast cardiac mri reconstruction via vsharp with auxiliary refinement network. In *International Workshop on Statistical Atlases and Computational Models of the Heart*, pages 183–192. Springer, 2024.
- [52] Syed Waqas Zamir, Aditya Arora, Salman Khan, Munawar Hayat, Fahad Shahbaz Khan, and Ming-Hsuan Yang. Restormer: Efficient transformer for high-resolution image restoration. In *Proceedings of the IEEE/CVF conference on computer vision and pattern recognition*, pages 5728–5739, 2022.
- [53] Syed Waqas Zamir, Aditya Arora, Salman Khan, Munawar Hayat, Fahad Shahbaz Khan, and Ming-Hsuan Yang. Restormer: Efficient transformer for high-resolution image restoration. In *Proceedings of the IEEE/CVF conference on computer vision and pattern recognition*, pages 5728–5739, 2022.
- [54] Jure Zbontar, Florian Knoll, Anuroop Sriram, Tullie Murrell, Zhengnan Huang, Matthew J Muckley, Aaron Defazio, Ruben Stern, Patricia Johnson, Mary Bruno, et al. fastmri: An open dataset and benchmarks for accelerated mri. *arXiv preprint arXiv:1811.08839*, 2018.
- [55] Xiaohua Zhai, Alexander Kolesnikov, Neil Houlsby, and Lucas Beyer. Scaling vision transformers. In *Proceedings of the IEEE/CVF Conference on Computer Vision and Pattern Recognition*, pages 12104–12113, 2022.
- [56] Kai Zhang, Wangmeng Zuo, Yunjin Chen, Deyu Meng, and Lei Zhang. Beyond a gaussian denoiser: Residual learning of deep cnn for image denoising. In *IEEE Transactions on Image Processing*, pages 3142–3155, 2017.
- [57] Lijun Zhang. “synapse profile 3472363”. <https://www.synapse.org/Profile:3472363>, 2025. Accessed: 2025-11-12.

7. Dataset Details

We train SDUM on a heterogeneous combination of CMRxRecon2024, CMRxRecon2025, and fastMRI multi-coil brain datasets, covering a broad range of anatomical targets, contrasts, and sampling patterns.

7.1. CMRxRecon2024

The CMRxRecon2024 [44] benchmark comprises two complementary tasks designed to evaluate contrast- and sampling-universal CMR reconstruction. Task 1 focuses on multi-contrast generalization under uniform undersampling, requiring a single model (up to three are allowed) to reconstruct a broad set of cardiac MRI sequences—including Cine, Aorta, Mapping, Tagging, and the unseen Flow2D and BlackBlood contrasts—acquired on a Siemens 3 T scanner. Data span multiple anatomical views (SAX, LAX, LVOT, aorta) and the published dataset includes 330 healthy volunteers (200 training, 60 validation, 70 test), totalling over 0.2 million k-space slices across six modalities. The released undersampling masks use $4\times$, $8\times$, and $10\times$ acceleration (ACS excluded). Task 2 evaluates robustness to diverse sampling schemes, using a single mandatory model to handle uniform, Gaussian, and pseudo-radial trajectories across accelerations from $4\times$ to $24\times$; the same cohort split applies, and all data are multi-coil raw k-space. Together, these tasks assess whether a model can generalize across contrasts, anatomical views, sampling patterns, and acceleration regimes, leveraging one of the largest publicly available multi-modality, multi-view cardiac k-space datasets. Together, these tasks assess whether a model can generalize across contrasts, views, sampling patterns, and acceleration regimes.

7.2. CMRxRecon2025

The CMRxRecon2025 [49] challenge advances universal cardiac MRI reconstruction by evaluating model robustness to real clinical distribution shifts across four subtasks. Two Regular tasks assess multi-center/multi-vendor generalization and multi-disease robustness, while two Special tracks test adaptation to unseen field strength (5T) and pediatric imaging. The full dataset comprises 600 volunteers with multi-parametric CMR imaging, divided into 200 training cases (from 5 centers, including both healthy volunteers and patients), 100 validation cases (from the same 5 derivation centers plus 1 new center), and 300 test cases (from the 5 derivation centers and more than 5 additional unseen centers). These cases span diverse contrasts (Cine, T1/T2 mapping, LGE, perfusion), sampling trajectories (Cartesian, Gaussian, radial), and field strengths (1.5T, 3T, 5T). By requiring a single model to perform consistently

across all subtasks without task-specific fine-tuning, CMRxRecon2025 pushes CMR reconstruction toward foundation-model-level generalization across centers, vendors, populations, and acquisition conditions.

7.3. fastMRI

The fastMRI Brain dataset [54] consists of 6,970 fully sampled multi-coil brain MRI scans acquired on 1.5T and 3T clinical scanners, covering four common contrasts: axial T1-weighted, post-contrast T1, T2-weighted, and FLAIR. Specifically, the dataset includes 3,001 volumes at 1.5T and 3,969 volumes at 3T, each providing raw multi-coil k-space in a vendor-neutral format suitable for supervised and semi-supervised reconstruction research. As one of the largest public multi-coil brain MRI datasets, fastMRI Brain offers a realistic and diverse testbed for assessing cross-contrast and cross-field-strength generalization in accelerated MRI reconstruction

8. Implementation Details

8.1. Network Architecture

Each cascade of SDUM consists of three tightly integrated components: a deep Restormer-based reconstructor, a coil-sensitivity map estimator (CSME), and a sampling-aware weighted data-consistency (SWDC) operator. The CSME is implemented as a Complex UNet with channel progression $\{12, 24, 48, 96, 192\}$, instance normalization, LeakyReLU activations, and deconvolution-based upsampling. The model operates on the fully sampled ACS region and outputs complex CSMs, which are explicitly normalized per spatial location using $x \leftarrow x / \sqrt{\sum_c |x_c|^2}$ to enforce $\sum_c |S_c|^2 = 1$, following standard SENSE practice.

The SDUM reconstructor is a two-level Restormer backbone configured according to the hyperparameters in our released codebase (see full config in the supplement). Each cascade receives a multi-frame complex input tensor (reshaped to $2T$ channels) and processes it through a shallow 3×3 stem ($10 \rightarrow 256$ channels), followed by two hierarchical Transformer levels with channel widths $\{256, 512\}$, attention heads $\{1, 2\}$, and block depths $\{3, 6\}$. All Transformer Blocks employ MDTA, GDFN feed-forward layers with expansion factor 3, and LayerNorm-based pre-normalization with Drop Path ($p=0.1$). Downsampling and upsampling are performed via PixelUnshuffle/PixelShuffle, and skip connections propagate encoder features to the decoder at matching resolutions. A refinement stage with Two additional Transformer Blocks further enhance the reconstructed output, followed by a 3×3 projection to restore multi-frame complex channels.

Table 5 | **Scaling of SDUM with respect to unrolled depth T .** PSNR increases consistently with cascade count, following approximately $\text{PSNR} \sim \log(\text{parameters})$. Training infrastructure refers to the number of NVIDIA H100 nodes (each with 8 GPUs).

T	PSNR (dB)	Parameters	Training Infra
1	28.73	42.16M	1-node (8×H100)
3	30.21	126.49M	2-node (16×H100)
6	32.09	252.97M	4-node (32×H100)
10	32.54	421.60M	8-node (64×H100)
18	33.18	758.91M	8-node (64×H100)

The reconstructor supports both *time conditioning* (cascade index) and *label conditioning* (sampling pattern, acceleration factor, and protocol type). Sinusoidal embeddings are transformed via a two-layer MLP and injected into every Transformer Block through additive channel-wise biases, enabling a shared model to adapt to heterogeneous acquisition settings. During unrolling, each cascade also receives cross-cascade skip features, allowing deeper cascades to reuse encoder/decoder outputs from previous cascades. Sampling-aware weighted data consistency (SWDC) is applied after each cascade using mask-specific learnable k-space weight maps, cropped to match the acquired resolution. The model operates on coil-reduced images. All operations use divisible padding aligned with the Restormer’s 2-level downsampling hierarchy. Complex-valued MRI inputs are processed as stacked real and imaginary channels, and all convolutions are real-valued. Across the full model, 18 cascades are instantiated, each containing an independent CSME module and a full Restormer block stack, with inter-cascade skip connections.

8.2. Training Procedure

We follow the progressive cascade-expansion schedule outlined in the main paper, gradually increasing model depth from $T=6$ to $T=10$ and finally $T=18$, with interior cascades warm-started at each stage. Training uses the Muon optimizer [21] with a base learning rate of 2.4×10^{-4} , cosine decay, weight decay of 1×10^{-3} , and an SSIM reconstruction loss. Each stage is optimized for roughly 20k steps. We employ mixed-precision training (BF16) and gradient checkpointing to reduce memory consumption, and the batch size is adaptively selected based on the input resolution and available GPU memory.

All data processing and augmentation are implemented based on MONAI [4] and performed directly in *k-space*. From the raw complex k-space input, we apply randomized transformations including axis-aligned flips, random k-space shifts, k-space phase shifts,

Table 6 | **Inference computation details across different input sizes.** Reported values are averaged per slice on a single NVIDIA H100 GPU.

Input Size	Inference Time (s)	GPU Memory (GB)
128×128	0.32	4.78
256×256	1.03	6.07
256×512	2.06	7.98
328×512	2.67	9.26
328×640	3.30	9.62
328×768	3.97	10.83

gamma-based complex contrast augmentation, and spatially varying k-space resize/crop, and simulated removal of readout oversampling. A randomized under-sampling mask is then applied using the unified operator, which samples from multiple mask families, each with independently randomized center fractions and acceleration factors. The masked k-space is inverted to generate aliased images, and the ground-truth target is obtained by inverse-FFT of the fully sampled k-space. Table 5 reports the compute infrastructure and performance scaling of SDUM with respect to unrolled depth T .

8.3. Inference Computation Details

SDUM performs inference in a single feed-forward pass without any iterative refinement, enabling fast and predictable deployment performance. Across a range of input resolutions commonly seen in CMR, the model exhibits near-linear scaling in both runtime and memory footprint (Table 6). On a single NVIDIA H100 GPU, inference on low-resolution slices (128×128) completes in 0.32 s using less than 5 GB of memory, while mid-range clinical resolutions (256×256 to 256×512) require 1.0–2.1 s and 6–8 GB. At the high-resolution end, a full 328×768 slice is reconstructed in 3.97 s with peak memory usage of 10.8 GB, allowing reliable inference even on a single-GPU deployment and suitable for near-real-time reconstruction pipelines.

9. Additional Experiment Results

9.1. Statistical Analysis and Comprehensive Comparison

To provide a rigorous statistical assessment of our proposed SDUM method, we conducted a comprehensive paired-difference analysis using PromptMR as the baseline across all validation cases from the CM-RxRecon 2024 Challenge. Figure 5 and 6 presents violin plots illustrating the distributions of ΔPSNR and ΔSSIM improvements for both Task 1 (uniform undersampling, $n = 1,614$) and Task 2 (kt-space undersampling, $n = 1,281$). The results demonstrate that

Paired Differences vs PromptMR Baseline (Task 1 (Uniform Undersampling))

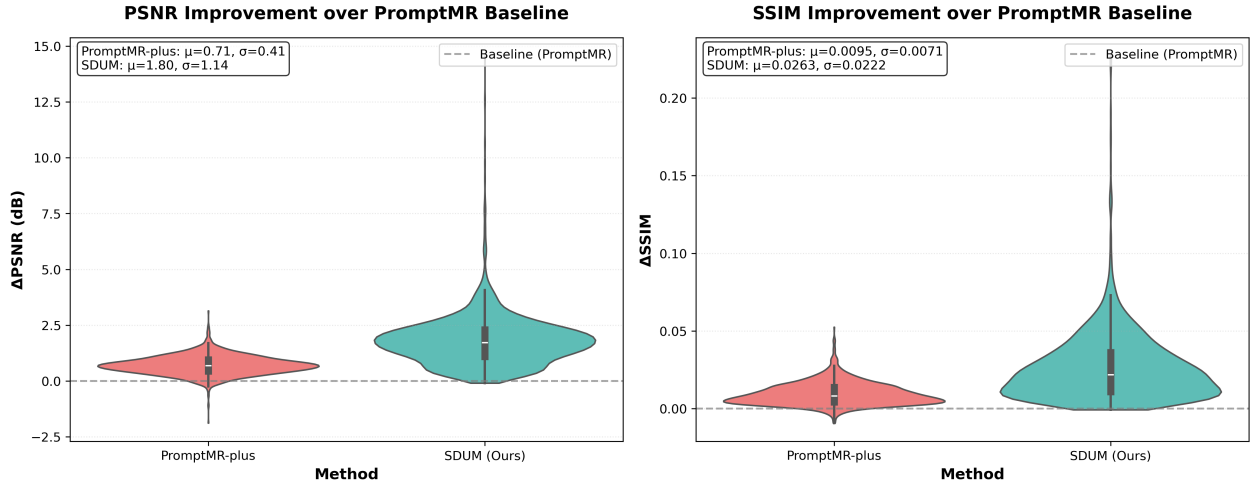


Figure 5 | Statistical comparison of PSNR and SSIM improvements over PromptMR baseline for Task 1 (Uniform Undersampling).

Paired Differences vs PromptMR Baseline (Task 2 (kt-space Undersampling))

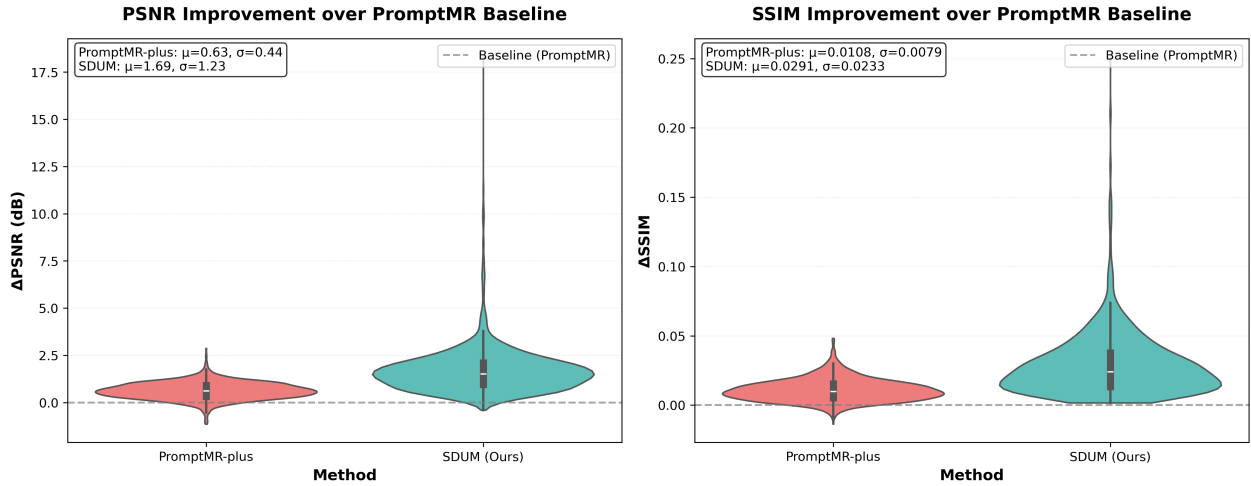


Figure 6 | Statistical comparison of PSNR and SSIM improvements over PromptMR baseline for Task 2 (kt-space Undersampling).

SDUM achieves substantially larger improvements over the baseline compared to PromptMR+ across both tasks. In Task 1, SDUM shows a mean PSNR improvement of 1.799 ± 1.142 dB versus 0.708 ± 0.413 dB for PromptMR+, representing a 1.091 dB advantage. This superiority is even more pronounced in SSIM, where SDUM achieves 0.0263 ± 0.0223 improvement compared to 0.00946 ± 0.00715 for PromptMR+ (advantage: $+0.01687$). Task 2 exhibits similar trends with SDUM demonstrating 1.685 ± 1.231 dB (PSNR) and 0.02907 ± 0.02333 (SSIM) improvements, surpassing PromptMR+ by 1.060 dB and 0.01827, respectively. Notably, the head-to-head comparison reveals that

SDUM outperforms PromptMR+ in 90.3% of Task 1 cases and an even more dominant 93.9% of Task 2 cases, indicating superior generalization to dynamic kt-space undersampling patterns. The larger standard deviations observed for SDUM reflect its ability to achieve substantial improvements in challenging reconstruction scenarios, while the consistently positive mean differences across both metrics and tasks provide strong statistical evidence for the robustness and effectiveness of our approach. The higher win rate in Task 2 suggests that SDUM's architecture is particularly well-suited for handling complex temporal undersampling schemes, which are more representative of clinical dy-

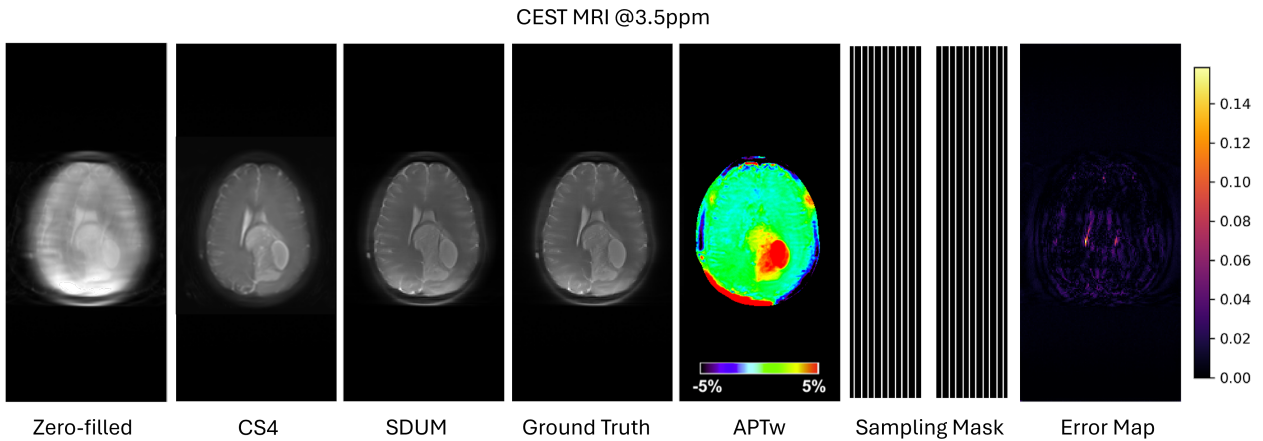


Figure 7 | **Zero-shot CEST MRI reconstruction on in-house data.** From left to right: zero-filled reconstruction from the $4\times$ undersampled multi-coil k-space, CS4 reconstruction from the scanner using the Philips commercial compressed sensing algorithm, SDUM, fully sampled reference, the derived amide proton transfer-weighted (APT_w) map at ± 3.5 ppm, the corresponding one-dimensional Cartesian sampling mask, and the per-pixel absolute error map between SDUM and the reference (values in the range $[0, 0.14]$). SDUM produces an image that is visually indistinguishable from the fully sampled reference and substantially reduces residual aliasing compared with CS4, achieving PSNR = 43.57 dB and SSIM = 0.9769 without any fine-tuning on this dataset.

namic cardiac MRI acquisitions. These statistical findings, combined with the qualitative results presented in the main paper, demonstrate that SDUM establishes a new state-of-the-art for multi-contrast cardiac MRI reconstruction across diverse undersampling strategies.

9.2. Zero-shot reconstruction of CEST MRI

Chemical Exchange Saturation Transfer (CEST) MRI scans were performed on an in-house brain dataset using a 3T scanner (Achieva, Philips Medical Systems, Best, the Netherlands) of patients with brain tumor. The body coil was used for excitation, and signal reception employed a 32-channel phased-array head coil (Invivo, Gainesville, FL). The CEST protocol used a saturation field strength B_1 of $2\mu\text{T}$ applied for 2 s, repetition time $\text{TR} = 6.5$ s, echo time $\text{TE} = 8.31$ ms, and slice thickness of 4 mm. Fully sampled multi-coil k-space data were acquired together with data retrospectively undersampled by a factor of four using Cartesian phase-encoding undersampling. The figure shows the magnitude image and APT_w map at the 3.5 ppm saturation offset, where CEST contrast manifests as subtle percent-level signal changes that are highly sensitive to reconstruction errors.

The Philips scanner, CEST pulse sequence, and image contrast were not present in the training data for SDUM, so this experiment constitutes a strict zero-shot test on an unseen vendor and protocol. As illustrated in Fig. 7, SDUM removes the strong aliasing artifacts visible in the zero-filled reconstruction and re-

covers finer structures and lesion contrast that are still degraded in the CS4 baseline, which corresponds to the vendor-provided Philips commercial compressed sensing reconstruction from the scanner. Quantitatively, SDUM attains 43.57 dB PSNR and 0.9769 SSIM with respect to the fully sampled reference, while preserving the fidelity of the downstream APT_w map. This demonstrates that our foundation model can generalize across scanners and pulse sequences and can support quantitative CEST imaging in a zero-shot fashion.